Thermo X

Science Exploration

Open Access Research Article

Raman thermometry indicates aggregation-induced localized hotspots in optical tweezers

Hongkai Zhang[1,2], Nan Zhang[1,2], Xiaona Huang[1,2], Yunsong Pang[4], Shijing Wu[1,2], Dezhao Huang[1,2,*], Yanan Yue[3,*]

[1]School of Power and Mechanical Engineering, Wuhan University, Wuhan 430072, Hubei, China.
[2]Institute for GONEO New Energy, Wuhan University, Wuhan 430072, Hubei, China.
[3]Department of Mechanical and Manufacturing Engineering, Miami University, Oxford, Ohio 45056, USA.
[4]National Key Laboratory of Materials for Integrated Circuits, Shenzhen Institute of Advanced Electronic Materials, Shenzhen Institute of Advanced Technology, Chinese Academy of Sciences, Shenzhen 518055, Guangdong, China.

***Correspondence to:** Dezhao Huang, School of Power and Mechanical Engineering, Wuhan University, Wuhan 430072, Hubei, China; Institute for GONEO New Energy, Wuhan University, Wuhan 430072, Hubei, China. E-mail: dhuang2@whu.edu.cn
Yanan Yue, Department of Mechanical and Manufacturing Engineering, Miami University, Oxford, Ohio 45056, USA. E-mail: yueyanan@hotmail.com

Received: June 15, 2026 **Accepted:** October 12, 2026 **Published:** October 12, 2026

Cite this article: Zhang H, Zhang N, Huang X, Pang Y, Wu S, Huang D, et al. Raman thermometry indicates aggregation-induced localized hotspots in optical tweezers. Thermo-X. 2027;3:202629. https://doi.org/10.70401/tx.2026.0037

Abstract

Gold nanoparticles (Au NPs) provide useful but difficult-to-measure heating in optical tweezers used for colloidal transport, assembly, optofluidics, and bubble-mediated manipulation. Here, we combine 60 nm Au NPs with 5 μm polystyrene (PS) microspheres in a dual-laser Raman optical-tweezers platform. Au NPs serve as heat sources and PS microspheres report the microscale temperature through their Raman spectra. The PS band near 1,000 cm^{-1} has a calibrated temperature coefficient of -0.0054 $cm^{-1}·K^{-1}$. For Au stock-dispersion fractions of 0, 0.3, and 1 vol.%, the temperature-power coefficients are 53.5 ± 10.9, 110.4 ± 23.8, and 170.3 ± 18.2 $K·W^{-1}$, respectively. At 1 vol.% Au suspension, extrapolation of the pre-bubble temperature-power relation to 0.341 W gives a PS-reported temperature of approximately 351 K, below the normal boiling point of water. Electromagnetic simulations show that normalized per-particle absorption increases from 1.00 for an isolated Au nanoparticle to 15.35 for a seven-particle cluster, supporting aggregation-induced nanoscale heating as a mechanism for bubble formation. The PS reporter thus gives the microscale thermal response, and the nanoscale hotspots associated with bubble formation are inferred, not measured directly.

Keywords: Optical tweezers, Raman thermometry, gold nanoparticles, photothermal control, bubble onset

1. Introduction

Optical tweezers use the gradient force of a tightly focused laser beam to confine and manipulate microscopic particles with submicrometre precision[1,2]. They have become a standard tool for probing Brownian motion, colloidal interactions, particle-surface forces, self-assembly, and biological processes. In colloidal systems, optical tweezers provide non-contact control of individual particles while allowing their motion and interactions to be monitored in real time. Advances in beam shaping and field control have extended this capability from dielectric microspheres to metallic and plasmonic nanoparticles. With suitable particle size, morphology, polarizability, and illumination, metallic nanoparticles can be trapped, transported, oriented, and assembled[3-5].

In liquids, the trapping beam also heats the surrounding fluid, substrate, and absorbing particles. At 1,064 nm, water absorption produces a measurable background temperature rise, whereas Au nanoparticles add a more localized thermoplasmonic contribution[6-8]. The resulting temperature field changes the viscosity and refractive index of the liquid and can drive thermophoresis, near-wall thermo-osmotic slip, and local flow. These effects alter particle trajectories, trap stability, aggregation, and particle-surface interactions. Sufficient local heating can also initiate bubble formation. Heating may destabilize a trap, but it can also be used to control transport and assembly. This coupling between optical force and heat has motivated a broad range of optothermal and thermoplasmonic manipulation strategies. Local heating has been used to extend capture ranges, drive long-range colloidal transport, assemble micro- and nanostructures, and manipulate biological and soft-matter objects under non-contact conditions[9-11]. However, excessive heating can weaken confinement, alter the flow field, damage biological samples, or trigger unwanted bubbles. Quantitative thermometry in the trapping region is needed when Au nanoparticles are used as both optically manipulated objects and nanoscale heat sources.

© The Author(s) 2026. This is an Open Access article licensed under a Creative Commons Attribution 4.0 International License (https://creativecommons.org/licenses/by/4.0/), which permits unrestricted use, sharing, adaptation, distribution and reproduction in any medium or format, for any purpose, even commercially, as long as you give appropriate credit to the original author(s) and the source, provide a link to the Creative Commons license, and indicate if changes were made.

Microscopy alone cannot determine the temperature in the trapping region. Similar particle motion, aggregation, or bubble formation can occur at different temperatures because these processes also depend on optical forces, fluid flow, and surface interactions. Fluorescence thermometry, thermoreflectance, interferometry, and Raman thermometry have all been used for micro- and nanoscale temperature measurements. Fluorescent probes can photobleach or perturb the suspension, whereas thermoreflectance is mainly suited to solid interfaces and commonly requires a reflective transducer. Temperature measurements in a liquid optical trap require an *in situ* probe that causes minimal disturbance to the particles and surrounding fluid. Raman thermometry meets these requirements by relating temperature to the position, linewidth, or intensity ratio of a Raman-active vibration[12-14]. Once calibrated, the shift of a selected band provides a direct spectroscopic temperature readout. The method has been applied to semiconductors, two-dimensional materials, polymers, biological samples, and individual optically trapped particles. Peak-position thermometry is particularly useful in a dynamic trap because it is less sensitive than intensity-based measurements to laser-power fluctuations, alignment, collection efficiency, and particle number[15]. Raman spectroscopy is also chemically selective and can be integrated directly with optical microscopy and optical tweezers.

Direct Raman thermometry of Au nanoparticles remains difficult. Bare Au does not possess a strong, isolated intrinsic Raman band that can be calibrated as a temperature marker. Its optical response is dominated by absorption, elastic scattering, and plasmon resonance. Au nanoparticles can enhance Raman scattering from nearby species, but the resulting surface-enhanced signal originates from molecules or materials near the metal surface rather than from the Au lattice itself[16-18]. Au particles can generate heat efficiently without providing a convenient Raman readout of that heat. Absorbed optical energy in Au nanoparticles is rapidly transferred to the electronic and lattice subsystems[19-21], and the resulting temperature gradients have enabled opto-thermoelectric, thermophoretic, and convection-assisted trapping and transport[22-24]. Previous measurements of heating in optically trapped Au particles have relied on dark-field spectroscopy, Brownian dynamics, or particle trajectories. These methods estimate Au-particle heating, but the temperature reported by a nearby Raman probe also depends on the number and arrangement of Au particles around it. These can change during trapping and aggregation. It is therefore necessary to establish how the nominal Au concentration affects the Raman-measured thermal response.

In this work, we use a dual-laser Raman optical tweezers platform and a mixed suspension of Au nanoparticles and PS microspheres to separate heat generation from temperature readout. A continuous-wave 1,064 nm beam traps the PS microspheres and recruits nearby Au nanoparticles, while a 532 nm beam excites the temperature-sensitive PS Raman signal. The nominal Au concentration determines the amount of absorber in the suspension. Local heating, however, depends on how many Au particles enter the focal region and whether they aggregate. We therefore calibrate the PS band, measure the power-dependent response at three nominal Au loadings, and use electromagnetic calculations to examine how aggregation changes optical absorption.

2. Methods

2.1 Optical manipulation of PS and Au particles

Commercial PS microspheres with a diameter of 5 μm were diluted to a working concentration of approximately 7 μg·mL^{-1}, corresponding to approximately 10^5 particles·mL^{-1}. Citrate-stabilized Au NPs with a nominal diameter of 60 nm were supplied as a 0.05 mg·mL^{-1} aqueous stock dispersion. The PS concentration was held constant in all samples, while the nominal volume fraction of the Au stock dispersion was set to 0, 0.3, or 1 vol.%. Throughout this work, vol.% denotes the volume fraction of the commercial Au stock dispersion in the final suspension rather than the physical volume fraction of metallic Au. The corresponding final Au mass concentrations are approximately 0, 0.15, and 0.50 μg·mL^{-1}. The nominal concentration does not specify the number or arrangement of Au particles near the reporter because trapping and aggregation change their local distribution.

We first evaluated whether the 1,064 nm field could confine the PS microspheres and recruit the Au NPs. The 5 μm PS sphere lies outside the Rayleigh regime, so the incident and scattered fields were expanded in vector spherical wave functions and related through the T matrix following Nieminen *et al.*[25]. The radial force is obtained from the dimensionless radial force efficiency Q_r as

$$F_r = \frac{n_m P}{c} Q_r \tag{1}$$

where F_r is the radial optical force, n_m is the refractive index of water, P is the trapping power at the sample, c is the speed of light, and Q_r is calculated from the T-matrix solution. As shown in Note S1 and Figure S1, the force vanishes on the beam axis and is restoring on either side. At a trapping power of 0.100 W, the maximum restoring-force magnitude is approximately 176 pN. This calculation predicts a restoring radial force on the PS sphere in the idealized model.

For the 60 nm Au NP, the particle radius is much smaller than the trapping wavelength, and the radial gradient force was estimated in the Rayleigh approximation[3]. The complex dipole polarizability and radial gradient force are given by

$$\alpha = 4\pi\varepsilon_0\varepsilon_m a^3 \frac{\varepsilon_p - \varepsilon_m}{\varepsilon_p + 2\varepsilon_m} \tag{2}$$

$$F_r = \frac{2\pi n_m a^3}{c} \mathrm{Re}\left(\frac{\varepsilon_p - \varepsilon_m}{\varepsilon_p + 2\varepsilon_m}\right) \frac{\partial I}{\partial r} \quad (3)$$

where α is the dipole polarizability, a is the Au-particle radius, ε_0 is the vacuum permittivity, ε_m and ε_p are the relative permittivities of water and Au, I is the local intensity, and r is the radial coordinate. Here, the permittivity of Au is complex, so the polarizability in Eq. (2) is also complex. Its real part determines the gradient force in Eq. (3), while absorption causes heating and contributes to radiation pressure[26]. For the 60 nm Au particle at 1,064 nm, the Rayleigh approximation is used to estimate the radial gradient force, rather than the total optical force. As shown in Note S2 and Figure S2, the force is again directed towards the beam axis, with a maximum restoring magnitude of approximately 0.096 pN at 0.100 W. Although this force is much smaller than that acting on the PS microsphere, it biases Au NPs towards the high-intensity region. This inward force, together with particle transport near the interface, may contribute to Au accumulation and aggregation.

2.2 Raman optical tweezers system design

Figure 1 shows the Raman optical-tweezers platform and the roles of Au NPs and PS microspheres in heat generation and temperature measurement. In Figure 1a, a continuous-wave 1,064 nm laser is reflected by a dichroic mirror and focused through an upper 50 × objective (NA = 0.50) to form a trap close to the quartz-water interface. The focus confines 5 μm PS microspheres and recruits nearby 60 nm Au NPs. A CMOS camera shares the upper optical path and records the focal region throughout the experiment, allowing stable trapping, Au accumulation, and bubble formation to be followed. The chamber is mounted on a translation stage with a nominal displacement resolution of 250 nm, so the trapped assembly can be released and re-established between measurements. The image inset shows a PS microsphere held at the focal position, confirming stable planar trapping near the interface.

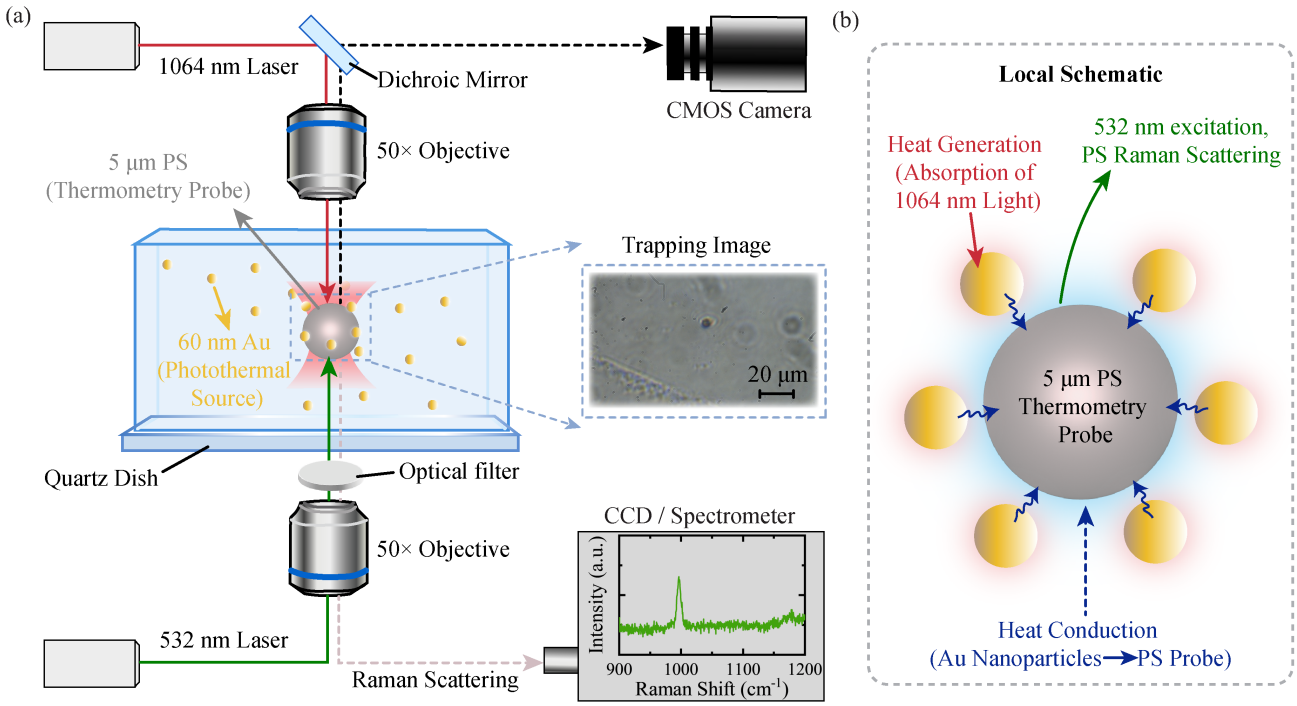

Figure 1. Dual-beam Raman optical tweezers platform and local thermal-sensing principle. (a) The upper path delivers the 1,064 nm trapping beam through a 50 × objective to confine 5 μm PS microspheres and recruit 60 nm Au NPs near the quartz-water interface; a CMOS camera records the trapping region. The lower path delivers the 532 nm Raman probe through a second 50 × objective, and the Stokes-shifted signal is filtered and collected by a CCD spectrometer. The image inset shows a trapped PS microsphere, and the spectral inset shows the characteristic PS Raman bands collected in the presence of the trapping beam; (b) Source-reporter concept: Au NPs absorb the 1,064 nm field and release heat to the surrounding water, while the PS ring-breathing mode near 1,000 cm^{-1} provides the Raman temperature readout. PS: polystyrene; Au NPs: gold nanoparticles; CMOS: complementary metal-oxide-semiconductor; CCD: charge-coupled device.

Raman thermometry converts the temperature-dependent spectral response of PS into temperature; the calibration relation and uncertainty propagation are given in Note S3. The aromatic ring-breathing band near 1,000 cm^{-1} was selected as the temperature marker because it is one of the strongest PS Raman features, is spectrally isolated from neighboring bands, and allows reproducible peak fitting. As the temperature increases, thermal expansion and anharmonic softening reduce the effective restoring force of the molecular vibrations, causing this band to shift toward lower wavenumber. Over the calibration range used here, the peak position is linear in temperature, and the temperature rise is obtained from

$$\Delta T = \frac{\Delta \omega}{\chi} \tag{4}$$

where Δω is the change in the fitted peak position and χ = dω/dT is the calibrated temperature coefficient. Raman excitation is introduced from below through a second 50 × objective. The 532 nm probe is aligned with the 1,064 nm focus, with a measured power of 8.36 mW and a spot diameter of approximately 60 μm at the sample. Each spectrum is integrated for 90 s. Peak positions were extracted by baseline-correcting the local 1,000 cm^{-1} band region and fitting the same Voigt profile form to all spectra. The estimated temperature rise due to water absorption is 3.50 × 10^{-4} K based on the Hale-Querry optical constants[27] (Note S4). This estimate includes only water absorption. Absorption of the 532 nm probe by nearby Au NPs is estimated in Note S4. The rise at the Au surface is about 0.2 K for an isolated particle and stays below 10 K for a seven-particle cluster. A filter stack rejects residual 1,064 nm trapping light and the 532 nm excitation line while transmitting the Stokes-shifted PS signal. Raman shifts from 900 to 1,300 cm^{-1} correspond to scattered wavelengths of approximately 559-572 nm, within the transmission window of the detection path. The spectral inset in Figure 1a shows the characteristic PS Raman band near 1,000 cm^{-1}, confirming Raman acquisition in the presence of the trapping beam. Figure 1b summarizes the thermal-sensing principle. The Au NPs absorb part of the 1,064 nm field and heat the surrounding liquid, whereas the PS microsphere reports the local thermal response through the position of its Raman band. The Au stock-dispersion fraction sets the amount of photothermal material available near the trap, while PS provides the Raman signal that bare Au lacks. The measured value is the temperature of the PS particles within the optical sampling region, not the temperature inside an Au nanoparticle or at an Au-Au contact.

3. Results and Discussion

3.1 PS Raman temperature calibration

Figure 2 shows the calibration of the temperature-dependent PS Raman band. In Figure 2a, PS microspheres supported on a silicon substrate are heated with a ceramic plate, while a thermocouple records the sample temperature. The 532 nm probe is held at 1.46 mW to minimize additional heating and particle displacement. Figure 2b shows the corresponding experimental arrangement. In Figure 2c, each curve represents the mean spectrum from three measurements, and the shaded band indicates the standard deviation among repeated measurements. The band near 1,000 cm^{-1} shifts steadily to lower wavenumber between approximately 20 and 92 °C, while retaining a similar line shape. A common Voigt profile can be used across the calibration range. The fitted peak positions in Figure 2d give χ = -0.0054 $cm^{-1}·K^{-1}$. The error bars are the peak-position uncertainties returned by the Voigt fits.

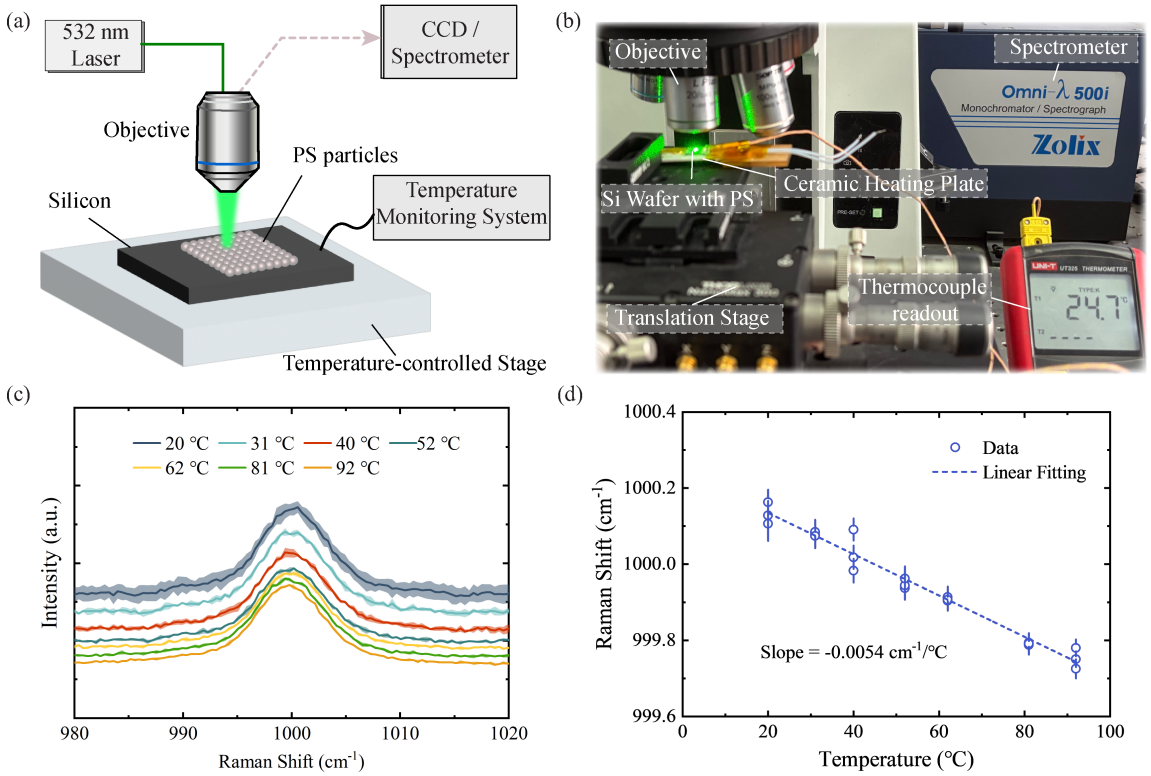

Figure 2. Calibration of PS Raman thermometry. (a) Schematic of the temperature-controlled Raman measurement; (b) Experimental calibration arrangement; (c) Baseline-corrected spectra acquired between approximately 20 and 92 °C; each curve is the mean of three measurements, and the shaded band indicates the standard deviation; (d) Linear redshift of the fitted PS band with temperature, giving χ = -0.0054 $cm^{-1}·K^{-1}$; error bars indicate the Voigt-fit uncertainty in peak position. PS: polystyrene.

To assess reproducibility, we compared the calibration used here with an independent PS Raman data set from our recent optical-tweezers study[28]. Ten measurements at each temperature gave a coefficient of -0.00485 $cm^{-1}·K^{-1}$, close to the present value of -0.0054 $cm^{-1}·K^{-1}$. We also measured PS particles in air and water at the same room temperature. The fitted peak positions were 1,000.28 ± 0.02 and 1,000.27 ± 0.02 cm^{-1}, respectively, with no resolvable solvent-dependent offset (Note S5 and Figure S3). However, this comparison does not establish that the temperature coefficient remains unchanged under simultaneous 532 and 1,064 nm illumination with Au NPs near the PS reporter. We assume that the calibrated coefficient remains applicable under these conditions. Nearby Au NPs may absorb the 532 nm probe and heat the reporter (by less than 10 K at the Au surface even for a seven-particle cluster, Note S4), and their near field may enhance signals from some regions of the PS sphere more than others. These effects could change both the temperature and the spatial weighting of the Raman signal. The spatial-weighting effect has not been independently quantified in the present work.

3.2 Composition-dependent thermal measurements

Figure 3 compares the Raman spectra of trapped PS microspheres at different Au stock-dispersion fractions. Figure 3a summarizes the measurement sequence: the PS concentration is fixed, the Au stock-dispersion fraction is set to 0, 0.3, or 1 vol.%, the PS microspheres are trapped at 1,064 nm, and Raman spectra are collected at 532 nm. Figure 3b,c,d show representative power-dependent spectra. In each composition, increasing trapping power shifts the PS band to lower wavenumber. The shift is weakest without Au and largest for the 1 vol.% sample. Figure 3e shows a representative Voigt fit with a peak center of 999.530 ± 0.052 cm^{-1}. The larger redshift after adding Au is consistent with increased absorption of the 1,064 nm trapping light near the PS microspheres.

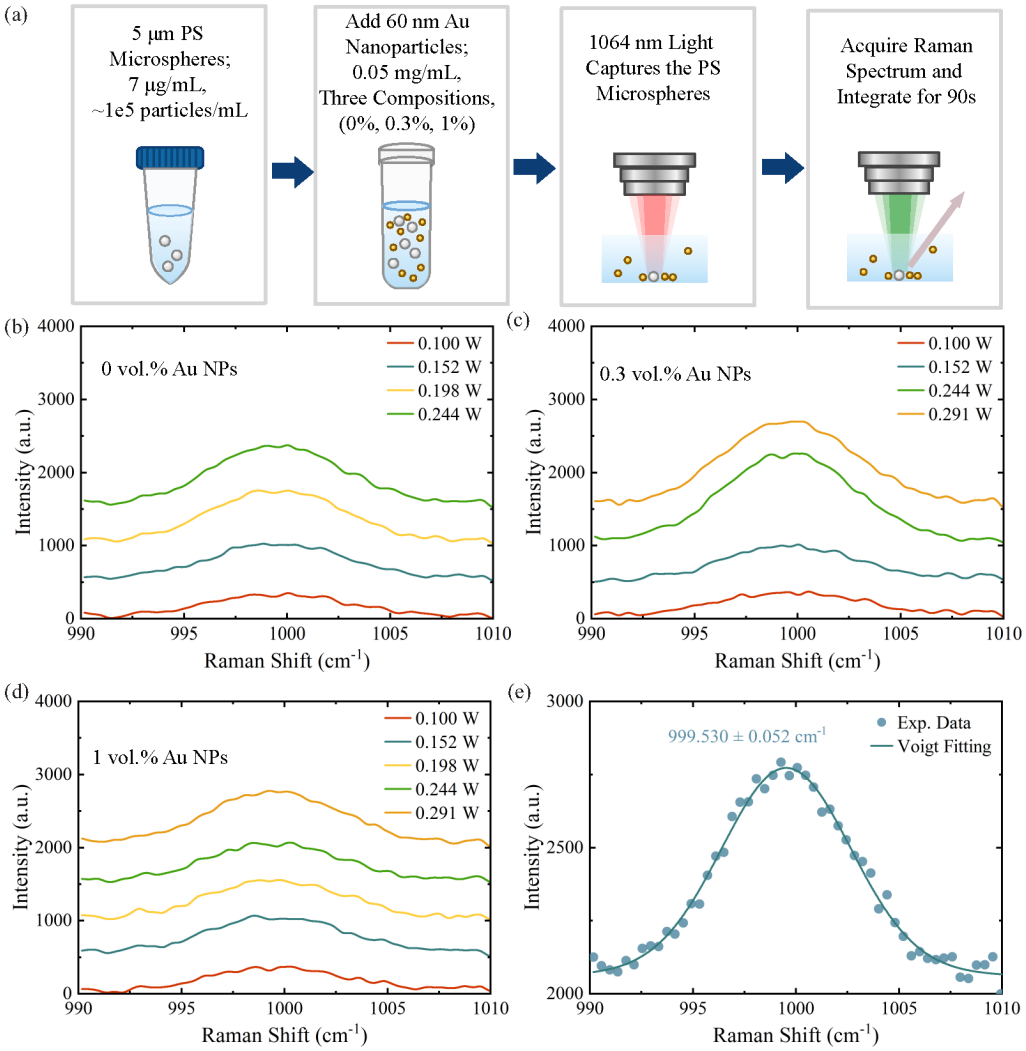

Figure 3. Raman measurement and spectral analysis. (a) Sample preparation and trapping sequence. (b, c, and d) Power-dependent PS Raman spectra for 0, 0.3, and 1 vol.% Au NP stock dispersion; spectra are vertically offset for clarity; (e) Representative Voigt fit used to determine the PS Raman peak position. PS: polystyrene; Au NPs: gold nanoparticles.

Figure 4 relates the Raman peak shifts to temperature. The Raman-shift-power slopes in Figure 4a,b,c are -0.29 ± 0.06, -0.60 ± 0.13, and -0.93 ± 0.10 $cm^{-1}·W^{-1}$ for 0, 0.3, and 1 vol.% Au stock dispersion, respectively. The temperature-power coefficients shown in Figure 4d, obtained from the calibrated Raman shifts, are 53.5 ± 10.9, 110.4 ± 23.8, and 170.3 ± 18.2 $K·W^{-1}$; their uncertainties reflect the regression uncertainty of the slope and do not include the calibration uncertainty of χ. The main source of uncertainty is the precision of the fitted peak position. The Voigt fits return peak positions with an uncertainty of about 0.05 cm^{-1}. Because the temperature coefficient of the PS band is small, this corresponds to about 10 K. For the Au-free sample, the redshift at 0.3 W is only about 0.09 cm^{-1}, comparable to this fitting uncertainty, so the relative uncertainty of the slope is largest for that sample. Additional contributions arise from the calibration uncertainty of χ, from the relatively large Raman spot (~60 μm), which averages signals from regions at different temperatures, and from changes in particle position and Au aggregation during the measurement. Applying the calibration under dual-beam illumination may also introduce systematic errors. At 0.291 W, the fitted temperature rises are approximately 16, 32, and 50 K. The temperature-power coefficient increases with Au loading (Figure 4e), indicating stronger heating of the PS reporter. Adding Au increases the amount of absorbing material available near the trap. Close particle spacing and aggregation can also enhance absorption through plasmon coupling[29-31], as examined in Figure 5d. Figure 4f illustrates this change. The response need not be proportional to the nominal concentration because particle capture, thermophoresis, near-wall flow, and aggregation change the number and arrangement of particles near the reporter.

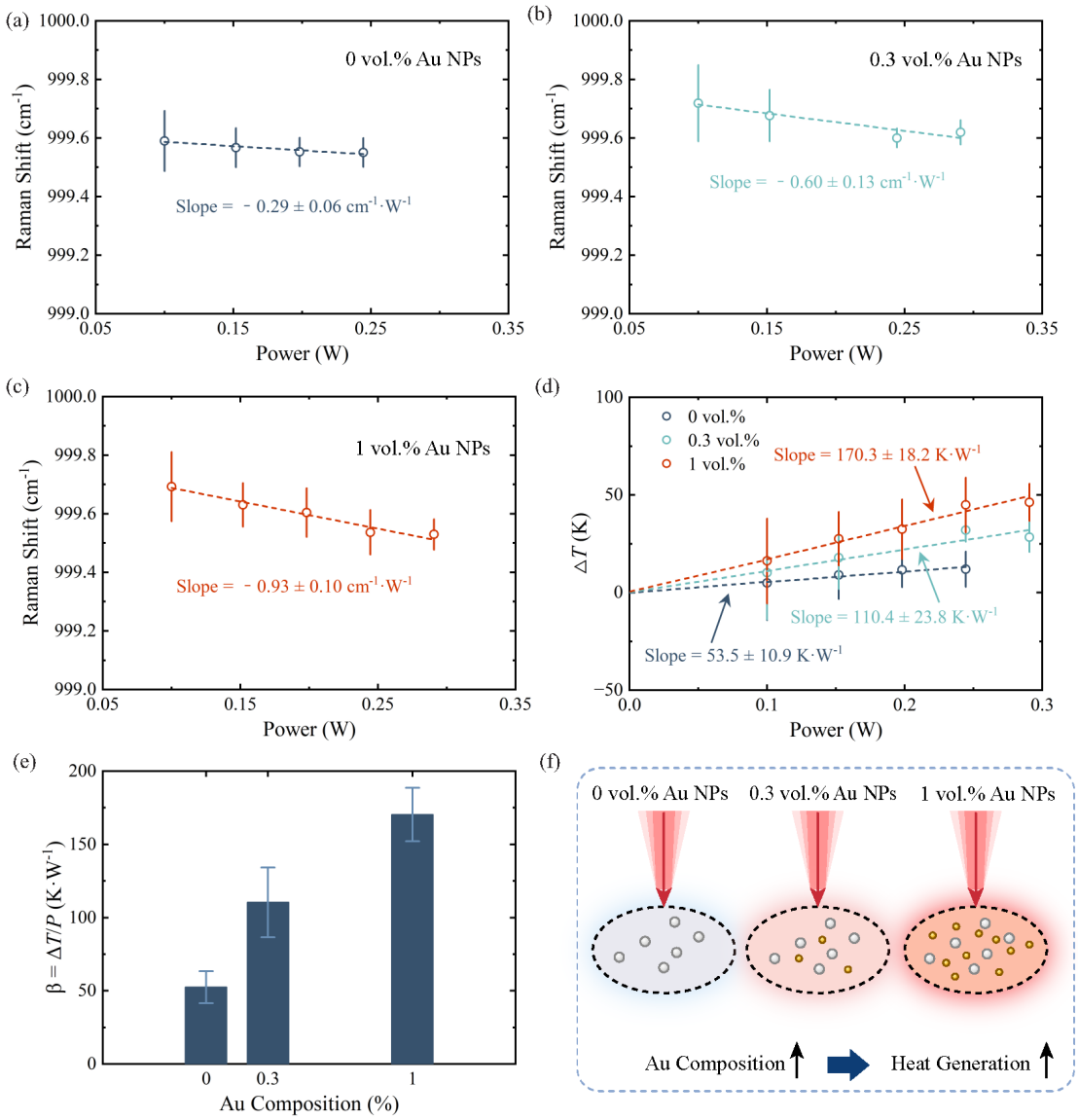

Figure 4. Composition-dependent Raman thermometry. (a, b, and c) Raman peak position as a function of trapping power for 0, 0.3, and 1 vol.% Au NP stock dispersion; (d) Temperature rise calculated from the PS calibration coefficient; (e) Temperature-power coefficient (β) as a function of nominal Au loading; (f) Schematic of increased optical absorption and heating at higher Au loading. Error bars in (a-d) arise from Voigt peak fitting; uncertainties in the slopes are from linear regression, and uncertainties in β are derived from the slope uncertainty only. The fitted coefficients increase with nominal Au loading. Au NP: gold nanoparticle; PS: polystyrene.

3.3 Au accumulation and bubble formation

We next examined bubble formation at higher trapping powers. Figure 5a illustrates particle accumulation and aggregation before bubble onset. The fits in Figure 4 describe the PS temperature response before a bubble forms. During these processes, optical forces act on both particle populations, and Au-induced heating can also change viscosity, thermophoretic drift, and near-wall transport[32-34]. Once a gas-liquid interface appears, Marangoni stress and bubble-driven flow alter the original trapping and heat-transfer conditions; bubble-state data were therefore excluded from the linear Raman analysis. To clarify the origin of bubble formation, we performed matched control experiments using pure Au-NP and pure PS dispersions. As discussed in Note S6 and Figure S4, in the Au-NP dispersion, particle accumulation was observed from both side- and top-view imaging, followed by bubble formation. In contrast, PS particles also accumulated under the same experimental conditions, but no bubble was observed. This comparison supports the role of Au-induced heating in bubble formation.

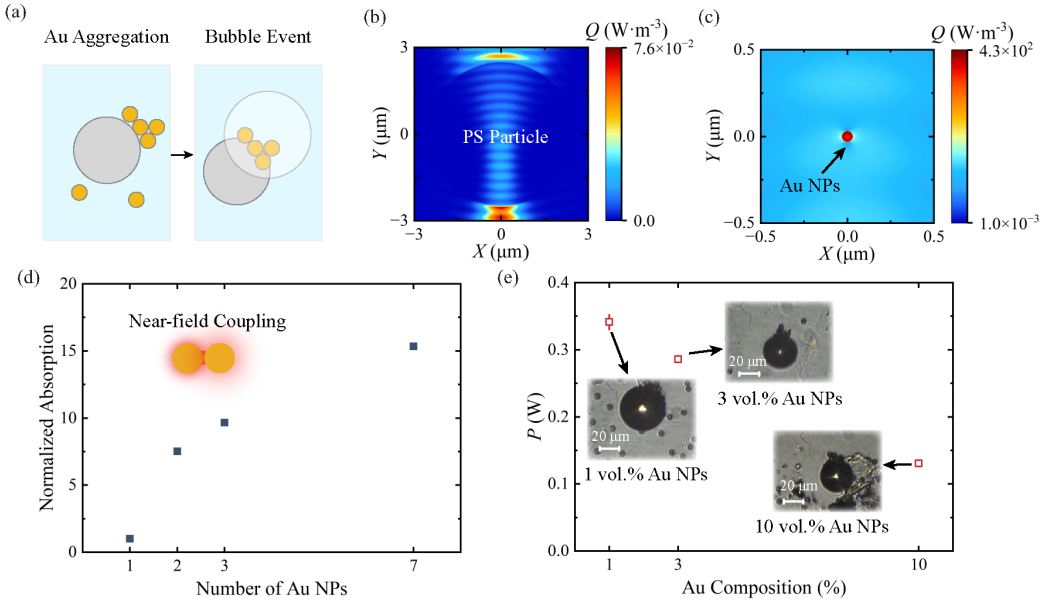

Figure 5. Au accumulation, electromagnetic loss, and bubble onset. (a) Schematic illustration of PS trapping, Au-rich accumulation, and subsequent bubble formation; (b, c) Electromagnetic loss-density distributions for isolated PS and Au particles; (d) Normalized per-particle absorption for N = 1, 2, 3, and 7; (e) Observed bubble-onset powers at 1, 3, and 10 vol.% Au stock dispersion; each concentration was tested in three independent trapping events on freshly loaded samples (n = 3). Error bars show the standard deviation of the three measurements. PS: polystyrene; Au NPs: gold nanoparticles.

To compare optical absorption, we used two-dimensional finite-element models with the electromagnetic waves, frequency-domain (EWFD) interface. The models used a 5 μm PS diameter, a 60 nm Au diameter, a laser wavelength (λ_0) of 1,064 nm, the ideal diffraction-limited Gaussian waist ($w_0 = \lambda_0/(\pi \cdot NA)$) of 0.677 μm, x-polarized illumination, and a unit-amplitude background field. Each geometry was centered at the same Gaussian waist. The loss-density distributions in Figure 5b,c show much stronger electromagnetic absorption in an isolated Au particle than in an isolated PS microsphere, which is consistent with the experimental observations. Because particle aggregation was observed prior to bubble formation in the experiments, we further examined optical absorption in Au aggregates. Aggregation was represented by clusters of touching Au particles with N = 2, 3, or 7 particles. The corresponding loss-density distributions are shown in Note S7 and Figure S5. For each geometry, the integrated loss was $Q_N = \iint_{A_{(Au,N)}} Q_h dA$, where Q_h is electromagnetic power dissipation density, and $A_{(Au,N)}$ is the area of N particles. The normalized per-particle value is $\eta_N = Q_N/(N \cdot Q_1)$, where Q_N is the area fraction of N particles, and Q_1 is the area fraction of an isolated particle. As displayed in Figure 5d, the resulting η_N values were 1.00, 7.51, 9.66, and 15.35 for the isolated particle, dimer, trimer, and compact seven-particle cluster, respectively. Values greater than 1 indicate the near-field electromagnetic coupling in the idealized touching clusters. These calculations show that aggregation enhances optical absorption in the modeled clusters, providing a mechanism for stronger local heating.

We then examined bubble onset at different Au concentrations. No bubble formation was observed at 0.3 vol.% Au within the available laser-power range. For each of the 1, 3, and 10 vol.% Au dispersions, three independent trapping events were performed on freshly loaded samples under the same nominal conditions. The bubble-onset powers were 0.341 ± 0.011, 0.286 ± 0.005, and 0.131 ± 0.004 W (mean ± SD, n = 3), respectively (Figure 5e). Possible sources of uncertainty include mechanical vibrations and fluctuations in laser power. The decrease in onset power with increasing Au concentration is consistent with stronger local heating. The 1 vol.% dispersion was the lowest concentration at which bubble formation was observed within the available power range. Repeated bubble-formation measurements are shown in Note S8 and Figure S6. Extrapolating the pre-bubble temperature-power relation to

the mean onset power of 0.341 W gives a PS-reported temperature of approximately 351 K. The PS reporter therefore remains below the normal boiling point of water at bubble onset. Its Raman signal averages the temperature over the reporter and the collection volume and does not resolve the local maximum next to an Au aggregate.

To compare the reporter temperature with an estimate near Au, we calculated the surface temperature of an isolated Au NP. In the Rayleigh limit[19,20], the absorption cross-section of a spherical Au nanoparticle is approximated by $C_{abs} = k_m Im(\alpha) = 4\pi k_m R^3 Im((\epsilon_{Au}-\epsilon_m)/(\epsilon_{Au}+2\epsilon_m))$, where $k_m = 2\pi n_m/\lambda_0$ is the wave vector of incident light, α, R is the radius of particles, ϵ_{Au} and ϵ_m are the dielectric constants of particles and surrounding medium, respectively. For comparison with the representative 0.337 W measurement, using R = 30 nm, λ_0 = 1,064 nm, n_m = 1.33, ϵ_{Au} = −41 + 3.5i, P = 0.337 W, and w_0 = 0.677 μm gives $C_{abs} = 3.50 \times 10^{-17}$ m², $I_0 = 2P/(\pi w_0^2) = 4.68 \times 10^{11}$ Wm⁻². Treating the Au nanoparticle as an isothermal sphere in an infinite water medium (Note S9), the steady surface temperature is 365 K. The estimated local temperature rise of approximately 72 K is higher than the approximately 57 K rise reported by the PS particle at the same power. This estimate illustrates why the temperature near Au can exceed the value reported by the 5 μm PS sphere. Electromagnetic coupling between neighboring Au particles can further concentrate absorption. The nearby PS sphere may also change the optical field and heat transfer. These effects support localized heating near Au aggregates, although the electromagnetic calculation alone does not determine the cluster temperature.

Other factors affecting bubble onset are discussed in Note S10. Nucleation depends on the local liquid temperature, dissolved gas, surface defects, interfacial pressure, and irradiation time[35-37]. For a localized heat source in an infinite liquid, the steady temperature rise is approximated by

$$\Delta T(r) \approx \frac{Q}{4\pi k_w r} \tag{5}$$

where Q is the absorbed power, k_w is the thermal conductivity of water, and r is the distance from the heat source[20]. For a fixed absorbed power, the temperature rise is larger close to the heat source and decreases with distance. The corresponding thermal diffusion time is

$$\tau_{th} \approx \frac{L^2}{\alpha_w} \tag{6}$$

where L is the characteristic length and α_w is the thermal diffusivity of water. For $L \approx 100$ nm, local equilibration is sub-microsecond, far shorter than the 90 s Raman integration. The Raman measurement therefore averages over temperature variations that occur on much shorter timescales and smaller length scales. Consequently, the stable and bubble-forming regimes should be treated separately. In the stable regime, the PS Raman peak reports the micrometre-scale thermal response of the trapped particles. Near bubble onset, heating close to Au aggregates may determine nucleation even though these regions contribute only part of the Raman signal. This interpretation is consistent with studies of plasmonic nanotweezers[38,39], hot particles[40], dynamic trapping and SERS hotspots[41-43], and Raman trapping[44,45].

4. Conclusion

In this work, we used PS microspheres as Raman thermometers to measure the thermal response of Au-containing optical traps, while the Au NPs served as photothermal absorbers. The PS band near 1,000 cm⁻¹ gives χ = −0.0054 cm⁻¹·K⁻¹. The fitted temperature–power coefficient increased from 53.5 ± 10.9 K·W⁻¹ without Au to 110.4 ± 23.8 and 170.3 ± 18.2 K·W⁻¹ at 0.3 and 1 vol.% Au stock dispersion. At 1 vol.% Au, the bubble-onset power was 0.341 ± 0.011 W. Extrapolating the pre-bubble temperature–power relation to 0.341 W gave a PS-reported temperature of approximately 351 K. This observation suggests that the microscale reporter temperature does not capture the local thermal conditions responsible for bubble nucleation. Electromagnetic finite element calculations under unit-amplitude excitation showed that normalized per-particle integrated absorption increased from 1.00 for an isolated Au nanoparticle to 15.35 for a compact seven-particle cluster. Together, the Raman measurements and electromagnetic simulations support aggregation-induced localized heating as a mechanism for bubble formation, but they do not directly measure nanoscale hotspot temperatures.

Future work will focus on improving temperature measurement precision and spatial resolution. Improved spectral stability and repeated calibration could reduce measurement uncertainty. The applicability of the calibration under dual-laser trapping conditions should also be tested through temperature-controlled measurements in water with and without nearby Au NPs. Varying the Raman excitation power at a fixed trapping power could help assess probe-induced heating. Reducing the Raman spot size and improving its overlap with the trapping region could reduce spatial averaging. Smaller Raman reporters and confocal detection could further limit contributions from surrounding regions. To probe nanoscale hotspots, tip-enhanced Raman thermometry could confine Raman excitation and detection near the tip apex. Alternatively, self-assembled monolayers of Raman-active molecules on Au surfaces could serve as local temperature reporters through surface-enhanced Raman scattering. These developments could improve the reliability of the present microscale measurements and enable more direct investigation of nanoscale hotspots involved in bubble formation.

Supplementary materials

The supplementary material for this article is available at: Supplementary materials.

Declarations

Acknowledgements

The authors declare that ChatGPT 6 was used solely for language polishing during the manuscript preparation process. All research content, including study design, data analysis, interpretations, figures, and tables, is original and was not generated using AI tools. The authors reviewed, revised, and approved the final manuscript and take full responsibility for its content.

Authors contribution

Zhang H: Conceptualization, methodology, software, validation, formal analysis, investigation, data curation, writing-original draft, writing-review & editing, visualization.
Zhang N, Huang X, Pang Y, Wu S: Validation, investigation, writing-review & editing.
Huang D, Yue Y: Conceptualization, methodology, software, validation, formal analysis, resources, writing-review & editing, supervision, project administration, funding acquisition.

Conflicts of interest

The authors declare no conflicts of interest.

Ethical approval

Not applicable.

Consent to participate

Not applicable.

Consent for publication

Not applicable.

Availability of data and materials

Data supporting the findings of this study are available from the corresponding authors upon reasonable request.

Funding

This work was supported by the National Natural Science Foundation of China (Grant Nos. 52576087, 92573103, and 52303093).

Copyright

© The Author(s) 2026.

References

1. Ashkin A, Dziedzic JM, Bjorkholm JE, Chu S. Observation of a single-beam gradient force optical trap for dielectric particles. Opt Lett. 1986;11(5):288-290. [DOI][PubMed]
2. Neuman KC, Block SM. Optical trapping. Rev Sci Instrum. 2004;75(9):2787-2809. [DOI][PubMed][PMC]
3. Svoboda K, Block SM. Optical trapping of metallic Rayleigh particles. Opt Lett. 1994;19(13):930-932. [DOI][PubMed]
4. Hansen PM, Bhatia VK, Harrit N, Oddershede L. Expanding the optical trapping range of gold nanoparticles. Nano Lett. 2005;5(10):1937-1942. [DOI][PubMed]
5. Selhuber-Unkel C, Zins I, Schubert O, Sönnichsen C, Oddershede LB. Quantitative optical trapping of single gold nanorods. Nano Lett. 2008;8(9):2998-3003. [DOI][PubMed]
6. Peterman EJG, Gittes F, Schmidt CF. Laser-induced heating in optical traps. Biophys J. 2003;84(2):1308-1316. [DOI][PubMed][PMC]
7. Andres-Arroyo A, Wang F, Toe WJ, Reece P. Intrinsic heating in optically trapped Au nanoparticles measured by dark-field spectroscopy. Biomed Opt Express. 2015;6(9):3646-3654. [DOI][PubMed][PMC]
8. Andrén D, Shao L, Odebo Länk N, Ać imović SS, Johansson P, Käll M. Probing photothermal effects on optically trapped gold nanorods by simultaneous plasmon spectroscopy and Brownian dynamics analysis. ACS Nano. 2017;11(10):10053-10061. [DOI][PubMed]
9. Chen Z, Li J, Zheng Y. Heat-mediated optical manipulation. Chem Rev. 2022;122(3):3122-3179. [DOI][PubMed][PMC]

10. Kollipara PS, Chen Z, Zheng Y. Optical manipulation heats up: Present and future of optothermal manipulation. ACS Nano. 2023;17(8):7051-7063. [DOI][PubMed][PMC]
11. Li F, Wei J, Qin X, Chen X, Chen D, Zhang W, et al. Thermo-optical tweezers based on photothermal waveguides. Microsyst Nanoeng. 2024;10(1):123. [DOI][PubMed][PMC]
12. Wu MY, Ling DX, Ling L, Li W, Li YQ. Stable optical trapping and sensitive characterization of nanostructures using standing-wave Raman tweezers. Sci Rep. 2017;7:42930. [DOI][PubMed][PMC]
13. Ai Y, Pan YL, Videen G, Wang C. Temperature measurement of trapped, thermally sensitive single particles in an optical trap using Raman spectroscopy. Appl Spectrosc. 2023;77(11):1300-1310. [DOI][PubMed]
14. Xu S, Fan A, Wang H, Zhang X, Wang X. Raman-based nanoscale thermal transport characterization: A critical review. Int J Heat Mass Transf. 2020;154:119751. [DOI]
15. Beechem T, Yates L, Graham S. Invited Review Article: Error and uncertainty in Raman thermal conductivity measurements. Rev Sci Instrum. 2015;86(4):041101. [DOI][PubMed]
16. McNay G, Eustace D, Smith WE, Faulds K, Graham D. Surface-enhanced Raman scattering (SERS) and surface-enhanced resonance Raman scattering (SERRS): A review of applications. Appl Spectrosc. 2011;65(8):825-837. [DOI][PubMed]
17. Stiles PL, Dieringer JA, Shah NC, Van Duyne RP. Surface-enhanced Raman spectroscopy. Annu Rev Anal Chem. 2008;1:601-626. [DOI][PubMed]
18. Langer J, Jimenez de Aberasturi D, Aizpurua J, Alvarez-Puebla RA, Auguié B, Baumberg JJ, et al. Present and future of surface-enhanced Raman scattering. ACS Nano. 2020;14(1):28-117. [DOI][PubMed][PMC]
19. Govorov AO, Richardson HH. Generating heat with metal nanoparticles. Nano Today. 2007;2(1):30-38. [DOI]
20. Baffou G, Quidant R. Thermo-plasmonics: Using metallic nanostructures as nano-sources of heat. Laser Photonics Rev. 2013;7(2):171-187. [DOI]
21. Munshi MAM, Chowdhury EH, Paniagua-Guerra LE, Dionne J, Giri A, Ramos-Alvarado B. A review of heat transport in solvated gold nanoparticles: Molecular dynamics modeling and experimental perspectives. Nanoscale. 2025;17(36):20803-20830. [DOI][PubMed]
22. Lin L, Wang M, Peng X, Lissek EN, Mao Z, Scarabelli L, et al. Opto-thermoelectric nanotweezers. Nat Photonics. 2018;12(4):195-201. [DOI][PubMed][PMC]
23. Liu S, Lin L, Sun HB. Opto-thermophoretic manipulation. ACS Nano. 2021;15(4):5925-5943. [DOI][PubMed]
24. Shukla A, Chand R, Boby S, Kumar GVP. Synchronized motion of gold nanoparticles in an optothermal trap. J Phys Chem C. 2025;129(11):5656-5665. [DOI]
25. Nieminen TA, Loke VLY, Stilgoe AB, Knöner G, Brańczyk AM, Heckenberg NR, et al. Optical tweezers computational toolbox. J Opt A: Pure Appl Opt. 2007;9(8):S196-S203. [DOI]
26. Harada Y, Asakura T. Radiation forces on a dielectric sphere in the Rayleigh scattering regime. Opt Commun. 1996;124(5-6):529-541. [DOI]
27. Hale GM, Querry MR. Optical constants of water in the 200-nm to 200-microm wavelength region. Appl Opt. 1973;12(3):555-563. [DOI][PubMed]
28. Zhang H, Yue Z, Liang M, Huang X, Zhang N, Xu L, et al. Quantifying dimensionality-dependent heating using *in situ* optical tweezer Raman thermometry. Phys Rev B. 2026;114(5):055403. [DOI]
29. Harris N, Arnold MD, Blaber MG, Ford MJ. Plasmonic resonances of closely coupled gold nanosphere chains. J Phys Chem C. 2009;113(7):2784-2791. [DOI]
30. Nam J, Won N, Jin H, Chung H, Kim S. pH-induced aggregation of gold nanoparticles for photothermal cancer therapy. J Am Chem Soc. 2009;131(38):13639-13645. [DOI][PubMed]
31. Fergusson J, Wallace GQ, Sloan-Dennison S, Carland R, Shand NC, Graham D, et al. Plasmonic and photothermal properties of silica-capped gold nanoparticle aggregates. J Phys Chem C. 2023;127(50):24475-24486. [DOI][PubMed][PMC]
32. Würger A. Thermal non-equilibrium transport in colloids. Rep Prog Phys. 2010;73(12):126601. [DOI]
33. Bregulla AP, Würger A, Günther K, Mertig M, Cichos F. Thermo-osmotic flow in thin films. Phys Rev Lett. 2016;116(18):188303. [DOI][PubMed]
34. Ji Y, Ren Y, Wang X, Qi H. Role of thermal effect on the capture stability of plasmonic optical tweezers. Case Stud Therm Eng. 2025;65:105559. [DOI]
35. Baffou G, Polleux J, Rigneault H, Monneret S. Super-heating and micro-bubble generation around plasmonic nanoparticles under cw illumination. J Phys Chem C. 2014;118(9):4890-4898. [DOI]
36. Wang Y, Zaytsev ME, Lajoinie G, The HL, Eijkel JCT, van den Berg A, et al. Giant and explosive plasmonic bubbles by delayed nucleation. Proc Natl Acad Sci USA. 2018;115(30):7676-7681. [DOI][PubMed][PMC]
37. Zhang H, Huang D, Li D, Huang X, Zhang N, Wu S, et al. Optical force-driven and tip-enhanced plasmonic bubble generation. Cell Rep Phys Sci. 2026;7(3):103192. [DOI]
38. Ren Y, Chen Q, He M, Zhang X, Qi H, Yan Y. Plasmonic optical tweezers for particle manipulation: Principles, methods, and applications. ACS Nano. 2021;15(4):6105-6128. [DOI][PubMed]
39. Crozier KB. Plasmonic nanotweezers: What's next? ACS Photonics. 2024;11(2):321-333. [DOI]
40. Ortiz-Rivero E, Orozco-Barrera S, Chatterjee H, González-Gómez CD, Caro C, García-Martín ML, et al. Light-to-heat conversion of optically trapped hot Brownian particles. ACS Nano. 2023;17(24):24961-24971. [DOI][PubMed][PMC]

41. Vosshage P, Otero CM, Schuknecht F, Huergo MA, Feldmann J, Lohmüller T. Dynamic trapping and printing of plasmonic dimers with optical vortex beams. J Phys Chem C. 2025;129(17):8262-8269. [DOI]
42. Fu W, Chi H, Dai X, Zhu H, Mesias VSD, Liu W, et al. Efficient optical plasmonic tweezer-controlled single-molecule SERS characterization of pH-dependent amylin species in aqueous milieus. Nat Commun. 2023;14(1):6996. [DOI][PubMed][PMC]
43. Dai X, Fu W, Chi H, Mesias VSD, Zhu H, Leung CW, et al. Optical tweezers-controlled hotspot for sensitive and reproducible surface-enhanced Raman spectroscopy characterization of native protein structures. Nat Commun. 2021;12(1):1292. [DOI][PubMed][PMC]
44. Penders J, Pence IJ, Horgan CC, Bergholt MS, Wood CS, Najer A, et al. Single particle automated Raman trapping analysis. Nat Commun. 2018;9:4256. [DOI][PubMed][PMC]
45. Zhang H, Huang D, Huang X, Zhang N, Wu S, Schiffbauer JE, et al. Tip-assisted Raman thermal probing and nanoscale trapping. Chin Phys Lett. 2025;42(8):080801. [DOI]

Publisher's Note

Science Exploration remains a neutral stance on jurisdictional claims in published maps and institutional affiliations. The views expressed in this article are solely those of the author(s) and do not reflect the opinions of the Editors or the publisher.